JOURNAL OF AIRCRAFT
Vol. 50, No. 5, September–October 2013

Dynamic Soaring of Sailplanes over Open Fields

Pritam P. Sukumar* and Michael S. Selig†
University of Illinois at Urbana–Champaign, Urbana, Illinois 61801

DOI: 10.2514/1.C031940

Dynamic soaring of a sailplane in the Earth's atmospheric boundary layer was computationally investigated over a range of conditions to explore the feasibility of sustained unpowered flight over open fields by taking advantage of wind shear. A point-mass sailplane model was studied, as well as a full six-degree-of-freedom piloted sailplane model. For the point-mass model, parameter sweeps were performed around a baseline 3-m (9.58-ft) wingspan sailplane having a weight of 15 kg (33 lb) and an aspect ratio of 20. Results from the point-mass model show that, in certain high-wind conditions, dynamic-soaring energy-conserving orbits are possible for flight trajectories extending from the ground to ≈200 m (656 ft) aloft. A six-degree-of-freedom piloted flight simulator was used, and it produced similar results that showed dynamic soaring over open fields for large vertical extents (extreme climb). Together, these results support the conclusion that it is possible to perform dynamic soaring in high-wind conditions through the atmospheric boundary layer to high altitudes over open land with model-scale unpowered sailplanes having both high wing loadings and high lift-to-drag ratios.

I. Introduction

SOARING can be defined as flight in which an internal thrust mechanism is not present. The aircraft thus needs to be capable of extracting energy from the atmosphere if it has to stay aloft. The earliest observations of soaring were made by Lord Rayleigh, based on the flight patterns of birds [1]. He hypothesized that the wind must be nonuniform in order to gain energy from the atmosphere. The flight of albatrosses in particular seemed to point toward a consistent mechanism for extracting energy from vertical wind gradients. The maneuvers involved in albatross flight were studied, and dynamic soaring as a mechanism for the extraction of energy from wind shear was investigated. Hendriks [2,3] showed that dynamic-soaring orbits that are periodic with respect to energy are possible.

Finding the minimum wind shear required to perform dynamic soaring posed a challenging numerical problem because of the coupled and nonlinear nature of the equations of motion. Optimal control was used to demonstrate that the shear commonly present over open seas was sufficient to allow an albatross to perform dynamic soaring [4]. Barnes [5] formulated classes of trajectories that simulated orbits flown by albatrosses in their daily flights. Lissaman [6] considered the cases of a step increase and continuous variation of wind speed in the boundary layer. He derived expressions for the minimum wind shear required for dynamic soaring in these conditions. More recently, Denny [7] studied dynamic soaring from a simplified point of view assuming a constant lift-to-drag ratio and dividing the trajectory into segments.

For full-scale aircraft, it was shown by Sachs and da Costa [8] that dynamic soaring by full-size sailplanes is possible with values of wind shear found near mountain ridges. Nonlinear optimal control methods have also been used to model dynamic soaring as an optimization problem with the final time and altitude as cost functions for full-size Unmanned Aerial Vehicles (UAV's) [9]. This approach for a full-sized UAV [9] was extended by Akhtar et al. [10], wherein they developed trajectory tracking algorithms that could be implemented in real time. Dynamic soaring for powered airplanes with the goal of minimizing the thrust required has been studied using parameter optimization [11]. Gordon [12] presented results from full-scale tests and computer simulations of an L-23 Super Blanik sailplane.

Use of dynamic soaring by humans has been largely limited to radio-controlled (RC) sailplanes because of the high flight speeds required in close proximity to the ground. As reported by Wurts [13], he pioneered RC sailplane dynamic soaring in wind shear developed on the leeward side of a windy ridge. Flight speeds near 322 km/h (200 mph) were reported by him. In an interesting article, Fogel [14] speculated on the possibility of dynamic soaring using RC sailplanes, apparently not aware that it had already been successfully performed. Since of this point, dynamic soaring of RC sailplanes has been an ongoing subject of research. Sachs and Mayrhofer [15,16] discussed optimal trajectories for RC-sized sailplanes flying in wind shear like that over a ridge. Wurts collaborated with Boslough [17], who conducted dynamic-soaring tests and computer simulations on a 2.4-m (8-ft) span RC sailplane. Parle [18] conducted preliminary flight tests with an RC sailplane and published data showing successful completion of energy-conserving oval trajectories. Pilots flying RC sailplanes in dynamic-soaring conditions over mountain ridges have continued to push flight speeds to higher limits. In fact, the current highest recorded speed is 801 km/h (498 mph).‡

As shown in this paper, rather than exploiting the effects of dynamic soaring to reach extreme flight speeds, the energy gain can be used to fly over nearly the entire vertical extent of the atmospheric boundary layer over open fields, that is, from ground elevation to surprisingly high altitudes [19]. Throughout the remainder of this paper, this kind of dynamic soaring will be called "extreme-climb dynamic soaring." A baseline three-degree-of-freedom (DOF) point-mass sailplane model is defined and used in an extreme-climb dynamic-soaring analysis. Trends are presented and discussed to illustrate the dependence of dynamic-soaring performance on both the aircraft and orbit-trajectory parameters. These results are extended to a full six-DOF real-time flight simulation to validate the possibility of performing piloted extreme-climb dynamic soaring over windy open fields like those found all over the Midwestern United States.

II. Point-Mass Dynamic-Soaring Model

A. Mathematical Formulation and Trajectory Prescription

The development of the method presented in this section closely follows that of Barnes [5]. The wind is assumed to be directed along

Presented at the AIAA Applied Aerodynamics, Chicago, 28 June 2010–1 July 2010; received 30 April 2012; revision received 17 September 2012; accepted for publication 24 September 2012; published online 9 July 2013.

*Graduate Student, Department of Aerospace Engineering, 104 South Wright Street. Member AIAA.
†Associate Professor, Department of Aerospace Engineering, 104 South Wright Street. Senior Member AIAA.

‡The top three speeds set by three different pilots for dynamic soaring with RC sailplanes are 716, 737, 801 km/h (445, 458, 498 mph). Data available online at http://www.rcspeeds.com/pilots.aspx [retrieved 17 September 2012].

the negative x axis from left to right. The equations of motion used in much of the research on dynamic soaring are those that model the aircraft as a point mass with three degrees-of-freedom [5,7,9,17,20]. The parameters are most conveniently expressed in the wind-aligned (wind-fixed) axis system [21] as

$$m\dot{U}\cos\gamma\cos\psi - mg\sin\gamma - D = m\dot{V} \tag{1}$$

$$L\cos\phi - mg\cos\gamma - m\dot{U}\cos\psi\sin\gamma = mV\dot{\gamma} \tag{2}$$

where γ is the flight path angle, ϕ is the bank angle, and ψ is the heading. The term $\dot{U}$ can be expanded as

$$\frac{\mathrm{d}U}{\mathrm{d}t} = \frac{\mathrm{d}U}{\mathrm{d}z}\frac{\mathrm{d}z}{\mathrm{d}t} = U'V\sin\gamma \tag{3}$$

The full term $m\dot{U}\cos\gamma\cos\psi$ on the left-hand side in Eq. (1) has been termed the "dynamic-soaring thrust" [5]. The name is used in this development because this force term increases the airspeed when the aircraft is gaining energy from dynamic soaring. The second term in Eq. (1) represents the force due to gravity, and the third term is the drag.

Although Barnes uses the term dynamic-soaring thrust in the wind-aligned axis for the aforementioned quantity $m\dot{U}\cos\gamma\cos\psi$ [5], the physical interpretation of $m\dot{U}\cos\gamma\cos\psi$ is not immediately easy to grasp. However, it is clear in the body-fixed system that the inertial speed and wind speed sum up to produce a relative wind that gives rise to forward tilting of the lift vector in the direction of flight (lift is perpendicular to relative wind). This effect is shown in Fig. 1. The component of this lift in the direction of flight produces in effect "thrust," that is, dynamic-soaring thrust. Whether this force is resolved in the wind-aligned or body-fixed system, it is this force that gives rise to energy extraction from wind shear, in this case, wind shear in an atmospheric boundary layer. As long as there is a misalignment between the relative wind and inertial speed, as shown in Fig. 1, there will be "thrust" that literally propels the airplane forward. But as the wind begins to overcome the sailplane and cause it to drift downwind against the headwind, the misalignment goes to zero, the energy extraction stops, and energy dissipation dominates again.

Continuing with the development in [5], the heading can be related to the velocity and wind-relative radius of curvature by

$$\dot{\psi} = \frac{V\cos\gamma}{r} \tag{4}$$

where r is the airplane-relative turn radius on the ground. The load factor and the bank angle are given by

$$n = \frac{(V/g)\dot{\gamma} + \cos\gamma + (U'V/g)\sin^2\gamma\cos\psi}{\cos\phi} \tag{5}$$

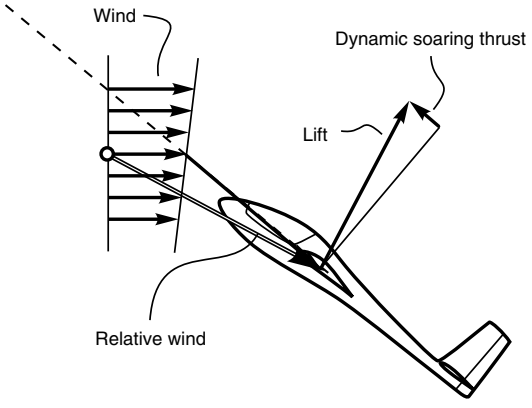

Fig. 1 Dynamic-soaring thrust (lift vector forward tilt) produced by the misalignment of relative wind and flight path trajectory.

$$\phi = \arctan\left[\frac{\dot{\psi} + U'\tan\gamma\sin\psi}{(\dot{\gamma}/\cos\gamma) + (g/V) + U'\sin\gamma\tan\gamma\cos\psi}\right] \tag{6}$$

The aircraft position in the ground frame can be found by integrating the velocities along the inertial axes. The velocities in this reference frame can be expressed in terms of the heading ψ, flight path angle γ, airspeed V, and wind speed U as

$$\dot{x} = -V\cos\gamma\cos\psi + U; \quad \dot{y} = V\cos\gamma\sin\psi; \quad \dot{z} = V\sin\gamma \tag{7}$$

For the aircraft to gain energy from dynamic soaring, the dynamic-soaring thrust term from Eq. (1) must be positive for a substantial portion of the orbit. Moreover, in that equation, it can be seen that, to satisfy this condition, the flight path angle should be positive when the aircraft is facing the wind and negative otherwise. Thus, the aircraft must ascend upwind in the atmospheric boundary layer and descend downwind on return: the "dynamic-soaring rule" [5]. Mathematically, this can be expressed by

$$-\pi/2 < \psi < \pi/2 \Rightarrow \gamma > 0; \quad \pi/2 < \psi < 3\pi/2 \Rightarrow \gamma < 0 \tag{8}$$

These equations of motion are solved for a family of prescribed trajectories to gain insight relating the sailplane parameters to dynamic-soaring performance. The prescribed trajectories used here are those parameterized by Barnes [5] and structured such that the aforementioned dynamic-soaring rule is enforced. To this end, the flight path angle γ is related to the heading angle ψ through a series of convenient transformations, each operating on the preceding one, viz.

$$\psi_1 = \psi + \frac{\pi}{2} \tag{9}$$

$$\psi_2 = 2\pi\left[\frac{\psi_1}{2\pi} - \mathrm{int}\left(\frac{\psi_1}{2\pi}\right)\right] \tag{10}$$

$$\psi_3 = \pi\left[1 - \cos\left(\frac{\psi_2}{2}\right)\right] \tag{11}$$

$$\gamma = \gamma_1\sin\psi_3 + \gamma_2\sin^2\psi_3 \tag{12}$$

Equation (9) introduces a phase shift of 90 deg in the heading ψ, and following that, Eq. (10) limits the angle to lie between 0 and 2π. Finally, Eq. (11) is a transformation that was included by Barnes [5] in order to model the dwell by the albatross when it is close to sea level. This trajectory "squash" causes the albatross to spend more time near the ground, and thereby, in Barnes' case, it causes the albatross trajectory model to skim the surface for a longer period of

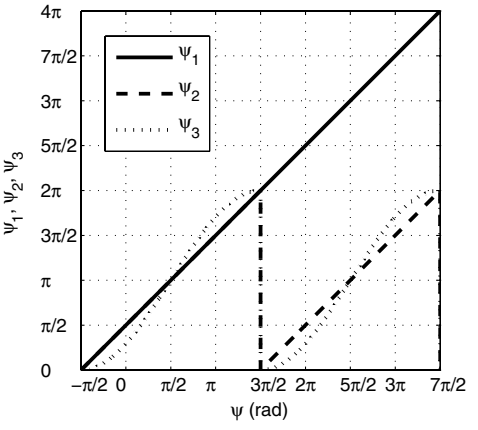

Fig. 2 Illustration of parameters used in transformation to define trajectory heading (two cycles shown).

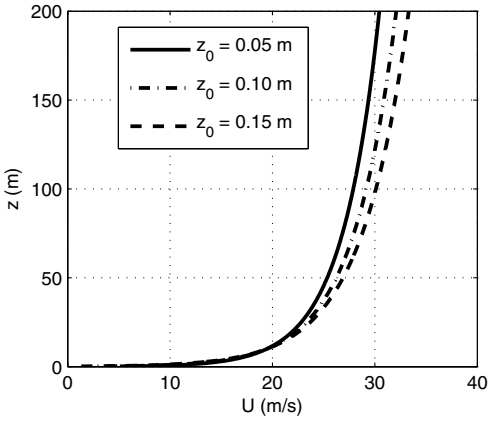

Fig. 3 Wind profiles for various roughness lengths ($U_{\text{ref}} = 19.44$ m/s and $z_{\text{ref}} = 10$ m).

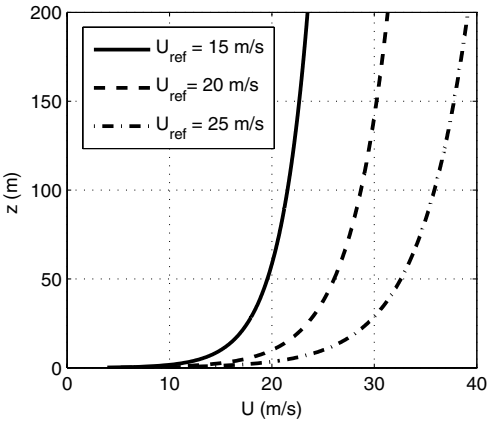

Fig. 4 Wind profiles for various reference wind speeds ($z_0 = 0.05$ m and $z_{\text{ref}} = 10$ m).

time and simulate albatross feeding behavior on the wing. The expressions given in Eqs. (9–11) are shown graphically in Fig. 2.

As can be seen in Eq. (12), γ_1 defines the maximum possible value for the flight path angle along the orbit. Thus, γ_1 has significant physical influence on the trajectory, and its effects will be explored later in Sec. IV. The parameter γ_2, when used, introduces a difference between the amplitudes of the climb and dive angles. Finally, the orbit begins above the surface at a prescribed height, which is called here the dwell height z_D.

B. Wind Shear Model

The wind shear in the atmospheric boundary layer has a significant impact on the dynamic-soaring performance. It is the shear that the airplane uses to gain energy when following a favorable dynamic-soaring trajectory. Thus, an accurate model of the wind profile is needed. A logarithmic profile (a profile commonly used in meteorological studies) was chosen as this is most applicable to measurements near the surface of the earth [22]. The logarithmic profile used is given by

$$U(z) = U_{\text{ref}} \frac{\log(z/z_0)}{\log(z_{\text{ref}}/z_0)} \tag{13}$$

where $U(z)$ is the wind speed at height z, and U_{ref} is the wind speed at the reference height z_{ref}. The variable z_0 is the aerodynamic roughness length or the roughness factor. It is an experimentally derived constant that accounts for the kind of surface over which the wind is blowing. Typically, a higher value of the roughness length indicates more obstructions on the surface, such as trees and buildings. Figure 3 shows the wind profiles for three values of the roughness coefficient with $U_{\text{ref}} = 19.44$ m/s (29.5 mph) and $z_{\text{ref}} = 10$ m (32.8 ft). As noted in [22], the wind profiles over open fields are matched well by a roughness factor of $z_0 = 0.05$ m, which is the value used throughout the remainder of this paper. Figure 4 shows the wind profiles for three values of the reference wind speed with $z_0 = 0.05$ m and $z_{\text{ref}} = 10$ m (32.8 ft). Although a reference wind speed of 25 m/s (55.9 mph) and above becomes extreme, sustained winds in the range 15 to 20 m/s (33.6 to 44.7 mph) are not uncommon. For instance, Table 1 shows sustained winds averaging near ≈15 m/s (33.6 mph) at Willard Airport, Champaign, IL,[§] on a specific day.

C. Numerical Solution Methodology

The equations of motion together with the system model that included the airplane, wind profile, and defined trajectory are solved iteratively, as outlined in the flowchart shown in Fig. 5. In the method, an orbit is defined as starting at the dwell height z_D in a banked turn, climbing into the wind to maximum height, then diving back downwind to the dwell height, albeit at some distance downwind relative to where it began. The entire formulation is framed around making the reference wind speed U_{ref} the dependent quantity such that an energy-conserving orbit is produced. Thus in the current method (which was implemented in MATLAB®), the iteration is performed on the reference wind speed U_{ref} until an energy-conserving orbit is obtained, that is, until the energy is the same at the orbit initial and final conditions. This primary orbit solver was included in a "wrapper" code that allowed for simultaneous sweeps on two parameters, with the mass always being one of the parameters. Many parameter sweeps were performed with the code, and these results are discussed later in Sec. IV.

The method was validated against results from Barnes [5], in particular, the "circular zoom" albatross case reported therein. For this particular case, the prescribed orbit trajectory produces a circular ground trace in the moving vehicle (albatross) frame of reference. Thus, if there was no wind, the prescribed trajectory ground trace would be a circle, thereby having a constant aircraft-relative turn radius.

The physical parameters used to model an albatross are defined as in Table 2. The specific wind model used by Barnes [5] is an exponential wind profile rather than the one used in the current results [see Eq. (13)]. For the Barnes wind model, the wind speed U at height z is given by

$$v = \frac{U}{U_{\text{ref}}} = 1 - e^{-a\zeta}; \quad \zeta = \frac{z}{z_{\text{ref}}} \tag{14}$$

where again the reference wind speed U_{ref} is given at the reference height z_{ref}. The parameter a defines the amount of wind shear. The specific values used by Barnes are given by

$$z_{\text{ref}} = 20 \text{ m}; \quad U_{\text{ref}} = 7 \text{ m/s}; \quad a = 7 \tag{15}$$

Finally, the initial conditions are defined by these dwell conditions:

$$V_D = 25 \text{ m/s}; \quad \psi_D = -\pi/2; \quad \gamma_D = 0; \quad x_D = 0; \quad y_D = 0; \quad z_D = 1.8 \text{ m} \tag{16}$$

The defining trajectory coefficients γ_1 and γ_2 are given by

$$\gamma_1 = \frac{\pi}{15}(12 \text{ deg}); \quad \gamma_2 = 0 \tag{17}$$

and the aircraft-relative turn radius r for the trajectory was set at 40 m.

The code runs with all of these parameters as input, iterates on U_{ref} to find the energy-conserving orbit (if one exists), and then saves the final three-dimensional (3-D) trajectory, resulting U_{ref}, and the orbit time history for one cycle. Figure 6 is the 3-D depiction of the orbit as seen by an inertial observer. In this graphic, a sketch of the albatross

[§]Data available online at http://www.atmos.uiuc.edu/weather/daily/index.html [retrieved 9 June 2010].

Table 1 Wind conditions at Willard Airport, Champaign, IL, on 29 April 2010 at 10 m height [23]

Time, hrs	Winds	Speed, m/s (mph)	Gusts, m/s (mph)	Visibility, km (mile)	Temperature, °F	Relative humidity, %
0953	S	13.86 (31)	17.43 (39)	16.09 (10)	66	43
1053	S	13.86 (31)	17.89 (40)	16.09 (10)	72	37
1153	S	14.76 (33)	18.33 (41)	16.09 (10)	73	36
1253	S	16.55 (37)	20.56 (46)	16.09 (10)	75	36
1353	S	14.76 (33)	23.47 (52)	16.09 (10)	77	36
1453	S	15.65 (35)	21.46 (48)	16.09 (10)	77	36
1553	S	15.20 (34)	21.01 (47)	16.09 (10)	79	36
1653	S	15.65 (35)	20.56 (46)	16.09 (10)	79	36
1853	S	15.65 (35)	19.67 (44)	16.09 (10)	73	36
1953	S	9.38 (21)	13.86 (31)	16.09 (10)	70	36

with a magnification factor of 5 is drawn every 3 s along the trajectory. Figure 7 shows the model albatross state characteristics as a function of heading ψ (as a surrogate for time). These results match the same case presented by Barnes and hence validate the computational method.

Briefly, Fig. 6 shows the resulting trajectory starting at the dwell conditions. At this particular moment, the albatross is flying crosswind before turning and climbing upwind. From the peak, the albatross flies downwind to a point further downwind than where it began. As Fig. 7 shows, the maximum airspeed V is near 25 m/s (55.9 mph) at the dwell condition. Interestingly, throughout the orbit, the total energy (energy height h_e) and lift-to-drag ratio L/D stay nearly constant. The load factor n reaches a peak near 2 before the dwell height and then unloads to a value of 1 at peak altitude. In maintaining near constant total energy, the balance between kinetic energy (wind relative) and height is clearly seen. The distance from start-to-finish is 69.8 m, taking 11.8 s for an average downwind transit speed of 5.9 m/s (13.2 mph).

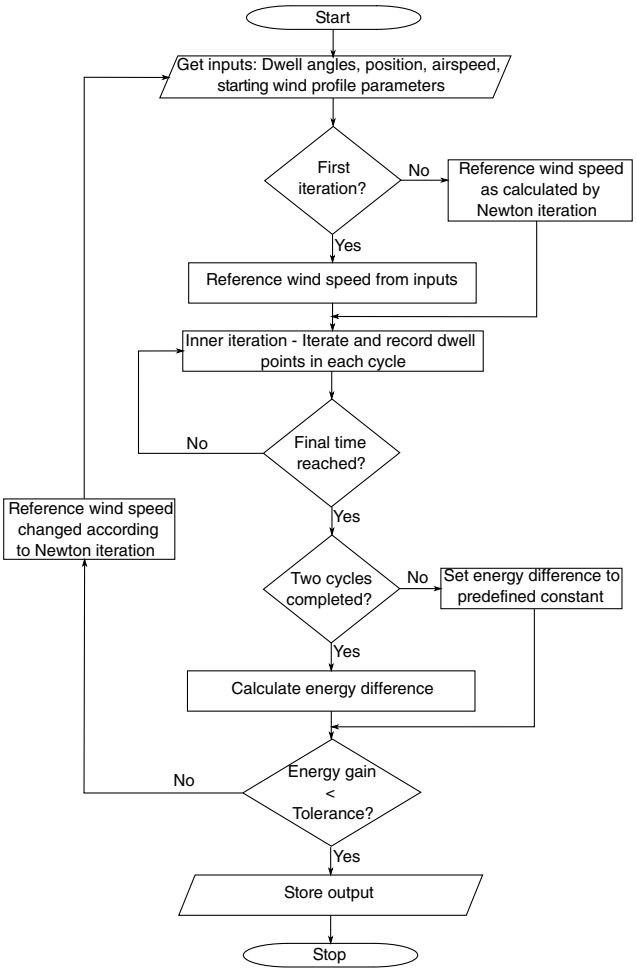

Fig. 5 Flowchart illustrating method to find energy-conserving orbit.

Table 2 Albatross physical characteristics for modeling dynamic soaring [5]

Parameter	Value
m	11 kg (24.25 lb)
m/S (W/S)	14.37 kg/m^2 (47.09 oz/ft^2
b	3.5 m (11.48 ft)
AR	16
e_o	0.9
C_{D_0}	0.015
$(L/D)_{\max}$	27.46

III. Extreme-Climb Dynamic Soaring: Baseline Case

The objective of this study was to investigate the feasibility of attaining high altitudes over open fields using dynamic soaring. A large parameter space was explored to define a baseline that ultimately achieved a high altitude of 185.1 m (607.3 ft). This exploratory process was based in part on experience gleaned while using a piloted real-time flight simulator discussed in Sec. V. The properties of the resulting sailplane, having a 3 m wingspan, are given in Table 3. It is representative of rather typical dynamic-soaring-capable sailplanes that are generally characterized by both high wing loadings and high maximum lift-to-drag ratios.

In defining the baseline orbit, practical considerations were taken into account in setting the dwell conditions. Flying in the strongest wind shear close to the ground is beneficial in dynamic soaring, but piloting skills must be considered. Experience has shown that a ground clearance of ≈2 m offers a skilled competition-level pilot enough margin for error when continuing along the orbit trajectory at high zoom speeds near the ground. With these factors in mind, a conservative baseline dwell height of 5 m was used. This height is the position of the aircraft center of gravity, yielding a tip clearance of 3.5 m for the 3-m wingspan baseline sailplane. The dwell speed was set at 65 m/s (145 mph), which is well within the capabilities of pilots having experience in dynamic-soaring conditions. Thus, the dwell conditions (initial conditions) for the prescribed orbit are

$$V_D = 65 \text{ m/s}; \qquad \psi_D = -\pi/2; \qquad \gamma_D = 0; \qquad x_D = 0; \qquad y_D = 0; \qquad z_D = 5 \text{ m} \tag{18}$$

The additional trajectory coefficients γ_1 and γ_2 were selected to be

$$\gamma_1 = 0.9(51.6 \text{ deg}); \qquad \gamma_2 = 0 \tag{19}$$

The high value for the flight-path-angle parameter γ_1 causes the aircraft to experience high wind shear that increases the dynamic-soaring thrust and aids in the achievement of an orbit with a large vertical extent [see Eq. (3)]. For this case, the airplane-relative circular turn radius r was set at 100 m. The wind profile model is that defined before by Eq. (13) with the values of the roughness coefficient and reference height given by

$$z_{\text{ref}} = 10 \text{ m}; \qquad z_0 = 0.05 \text{ m} \tag{20}$$

Newton iteration was used to solve for the required reference wind speed U_{ref} that yielded an energy-conserving orbit for the conditions prescribed. The resulting reference wind speed was found to be 19.44 m/s, as illustrated in Fig. 3.

The resulting dynamic-soaring orbit and corresponding time histories through one cycle are shown in Figs. 8 and 9. As seen, the climb is extreme (reaching a height of 185.1 m). The 200-m orbit width is consistent with the prescribed 100-m orbit radius. The aircraft travels a net downwind distance of 445 m over a period of 16.2 s, giving an average downwind travel speed of 27.5 m/s (61.5 mph). Throughout the entire cycle, the sailplane must in effect crab into the wind, which accounts for the odd-looking orientation of the aircraft relative to the flight path trajectory. From the view angle used to render Fig. 8, the crab is most apparent near the point of maximum height.

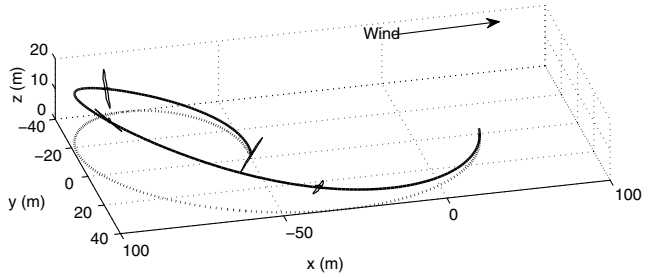

Fig. 6 Trajectory of an albatross performing dynamic soaring (albatross graphics model magnified five times normal size and drawn every 3 s).

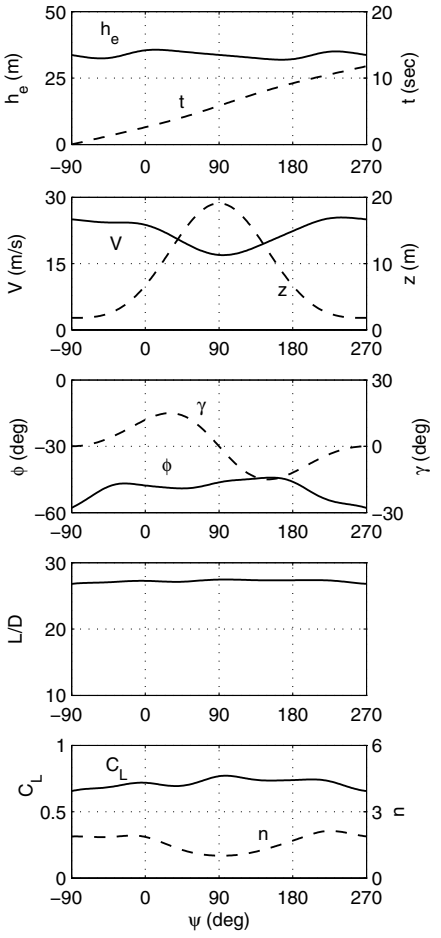

Fig. 7 Albatross dynamic-soaring orbit parameters for one orbit (see Fig. 6).

Table 3 Baseline sailplane characteristics for extreme-climb dynamic soaring

Parameter	Value
m	15 kg (33.07 lb)
m/S (W/S)	33.33 kg/m^2 (109.22 oz/ft^2)
b	3 m (9.84 ft)
AR	20
e_o	0.9
C_{D_0}	0.020
$(L/D)_{\max}$	26.59

Comparing the orbit parameters through one cycle shown in Fig. 9 with the Barnes case in Fig. 7, it can be seen that the lift coefficient is lower than that for the albatross case, which is in part due to the fact that the aircraft is flying at higher speed. The bank angle is higher,

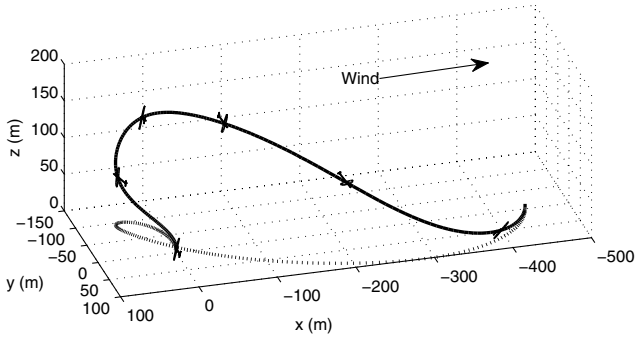

Fig. 8 Sailplane trajectory for extreme-climb dynamic soaring (sailplane model magnified 10 times normal size and drawn every 3 s).

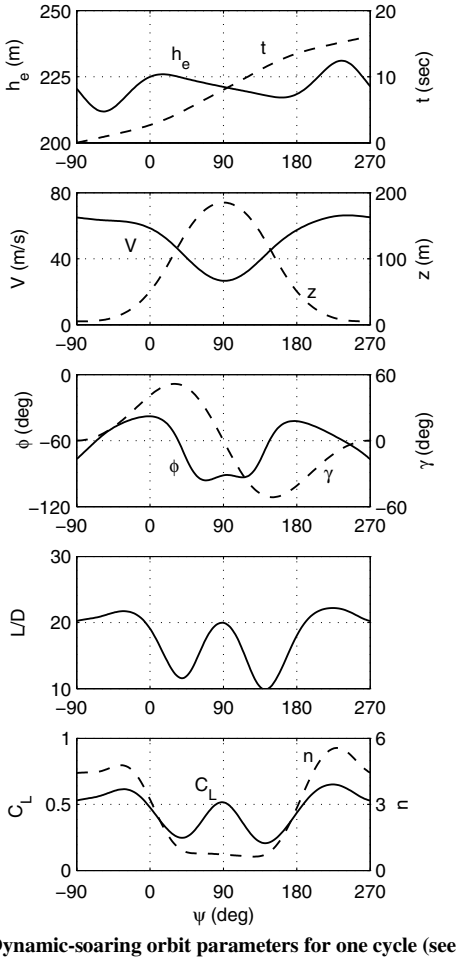

Fig. 9 Dynamic-soaring orbit parameters for one cycle (see Fig. 8).

resulting from the high speeds and radius of curvature required, which together result in a higher load factor. Overall the lift-to-drag ratio, load factor, and other time history data show greater variation than for the albatross case. The load factor n peaks near 6 at the end of the cycle before reaching the dwell height and thereafter turning away from the ground to repeat the cycle. Clearly, the high load factor and high speed over the orbit are not representative of any dynamic soaring by birds in nature. From a practical standpoint, however, the trajectory and physical characteristics along the path are not extraordinary, apart from the unexpectedly high altitude achieved while climbing upwind.

IV. Parameter Sweeps

In this section, parameter sweeps around the previous baseline are performed to explore the design space that can give rise to extreme-climb dynamic soaring. The baseline values and the sweep ranges for the individual parameters are shown in Table 4. The aircraft and orbit parameters used in the baseline dynamic-soaring case are included in every sweep case. The sweep ranges for individual parameters were chosen so as to encompass a wide range to better define and outline the feasible design space, while being physically realizable. Two-parameter sweeps were performed with mass always being one, and the other (see Table 4) was selected in turn from the following list: aspect ratio, parasite drag coefficient, dwell speed, dwell height, orbit flight-path-angle parameter, and orbit radius. The mass was chosen as the common parameter among all the plots because it is a physical parameter that gives an intuitive indication of the physical size of aircraft that is being used. The latter three (dwell height, orbit flight-path-angle parameter, and orbit radius) affect the final orbit altitude because they define the trajectory relative to the aircraft, whereas for the others (aspect ratio, parasite drag coefficient, dwell speed), the maximum orbit height is set by the baseline values yielding the maximum height of 185.1 m for an orbit starting at the baseline dwell height of 5 m. For all cases, the Oswald efficiency factor and the flight-path-angle parameter γ_2 were fixed at the baseline values ($e_o = 0.9,\ \gamma_2 = 0$). Finally, it should be mentioned that actual tradeoffs specific to a particular constrained design would include parameter coupling that has not been considered here, e.g., the connection between the Oswald efficiency factor and the parasite drag coefficient by way of the airfoil selection.

As before, the numerical solution was framed to yield the required reference wind speed, giving rise to energy-conserving dynamic-soaring orbits. Thus, the reference wind speed is the primary dependent quantity of interest in all cases. In the graphics presented, the reference wind speed U_{ref} scale was stopped at 35 m/s to completely show the trends with the parameter sweeps, but it must be realized that speeds in this range and above are rarely attained over open fields in conditions amenable to piloted dynamic soaring. In cases in which the orbit trajectory changes, the maximum altitude is also a dependent quantity, and these data are presented as well.

It is worth mentioning that for all orbits in this section (and before) the aircraft stays within the boundary layer. Also, in cases in which an increase or decrease of a baseline parameter resulted in a physically unrealizable energy-conserving orbit, the baseline parameter was chosen as the upper or lower bound for that sweep case. These baseline-bounded sweep cases correspond to those with "–" given in Table 4.

Table 4 Baseline and lower/upper bounds for aircraft and trajectory parameters

Parameter	Lower bound	Baseline	Upper bound
m, kg	6	15	—
b, m	—	3	4.2
AR	15	20	25
C_{D_0}	0.015	0.020	0.025
V_D, m/s	64	65	80
z_D, m	3	5	8
γ_1	0.4 (22.9 deg)	0.9 (51.6 deg)	—
r, m	60	100	110

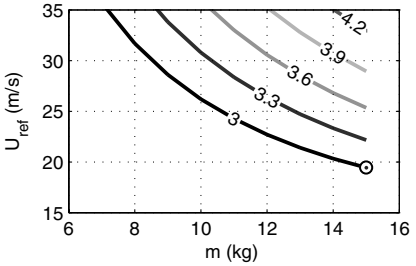

Fig. 10 Dynamic-soaring reference wind speed as a function of sailplane mass for various wingspans b ranging from 3 to 4.2 m with aspect ratio held constant.

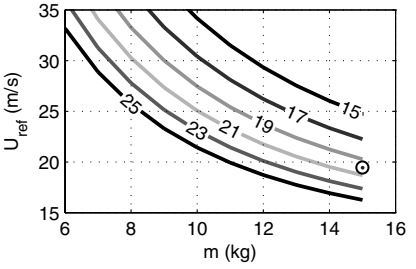

Fig. 11 Dynamic-soaring reference wind speed as a function of sailplane mass for wing aspect ratios AR ranging from 15 to 25 with wingspan held constant.

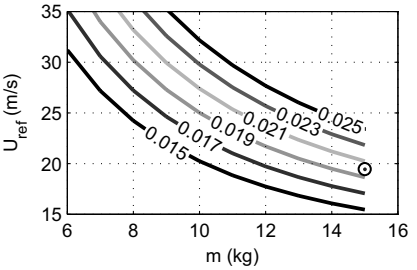

Fig. 12 Dynamic-soaring reference wind speed as a function of sailplane mass for various C_{D_0} values.

A. Effects of Aircraft Properties

Figures 10–12 show the required reference wind speed for changing aircraft mass along with span, aspect ratio, and parasite drag coefficient, respectively. In all figures, the baseline case is shown for comparison by a single circle symbol. What is immediately clear is that increasing mass lowers the required reference wind speed for sustaining energy-conserving dynamic-soaring orbits. In fact, as all trends indicate, the mass of the baseline case is the most favorable, and clearly a higher mass would further reduce the required wind speed.

The effect of higher mass is consistent with prior studies indicating that high wing loading is beneficial to dynamic-soaring performance [3,4,20]. The reason for this relates back to Fig. 1, which shows the main driver behind dynamic-soaring thrust. The longer a sailplane can penetrate into the wind, the more time there is for dynamic-soaring thrust to be produced and thereby increase the aircraft energy and sustain the perpetual orbit. Thus, sailplanes with higher mass (higher wing loading) are able to more efficiently sustain the condition (penetration into the wind) that gives rise to dynamic-soaring thrust.

In each of these cases, the trajectory "schedule" is the same; that is, the flight path angle along the orbit as a function of heading ψ is the same, and also the circular orbit relative to the aircraft is the same ($r = 100$ m). Consequently, the maximum height of the orbits is constant and equal to the baseline (185.1 m), and the width of the orbit is constant (200 m) for all data represented in Figs. 10–12. Because the higher wing loading cases all trend toward requiring less wind to

achieve the same maximum altitude of 185.1 m, they are said here to be more "efficient." Thus, reference here to higher efficiency dynamic soaring relates to a lower required wind speed to sustain dynamic soaring.

The effects of sailplane span shown in Fig. 10 are a direct result of changes in wing loading. For a given aircraft mass, decreasing the span with fixed aspect ratio (AR = 20) results in a lower wing area and consequently a higher wing loading. The trends show that a span smaller than the baseline would be even more efficient. It must be considered, however, that a smaller span would correspond to a smaller airplane with what might become an exceptionally high weight. At some point with such a high wing loading, managing to launch and land such an airplane could prove to be one of the largest challenges to successful extreme-climb dynamic soaring.

Figure 11 shows the effects of changing aspect ratio (wingspan held constant) and changing mass as the second parameter. The result is clear that higher aspect ratios yield higher values for $(L/D)_{\max}$. Consequently, with higher aspect ratios, less energy is lost due to drag, and thus, dynamic soaring becomes more efficient with a lower required wind speed. For reference, as shown in Table 5, the $(L/D)_{\max}$ ranges from approximately 23 to 30 for aspect ratios of 15 to 25, respectively.

Lowering the parasite drag coefficient C_{D_0} as shown in Fig. 12 produces results similar to those for increasing aspect ratios because of the direct effect of improving $(L/D)_{\max}$. As Fig. 12 shows, a sailplane configured like the baseline but with $C_{D_0} = 0.015$ yields a reference wind speed near 15 m/s. The value $C_{D_0} = 0.015$ is reasonable for a high-performance model-scale sailplane. For reference, as shown in Table 6, the $(L/D)_{\max}$ ranges from approximately 24 to 31 for parasite drag coefficients of 0.025 to 0.015, respectively.

For all cases, the maximum load factor was between approximately 5 and 7 and occurred near $\psi \approx 225$ deg (similar to the case shown in Fig. 9). This point in the orbit corresponds to the highest airspeed, which was between approximately 66 and 71 m/s for all cases (with the maximum being 70.89 m/s corresponding to the case in Fig. 10 with $m = 15$ kg and $b = 4.5$ m). Also, the highest lift coefficient encountered over all the cases was 0.9, which thereby avoids stall for a typical dynamic-soaring sailplane configuration and corresponding airfoil selection.

B. Effect of Initial Condition: Dwell Speed

Figure 13 shows the effects of changing the dwell speed, which is the initial orbit speed. As before, all other parameters are held constant, apart from the sweeping mass. Generally, a higher dwell speed increases the speed around the entire orbit, and to sustain this higher speed, more wind shear is required. Consequently, a higher reference wind speed results from increasing the dwell speed as shown in Fig. 13. At a dwell speed much below 64 m/s, the solution for the highest mass does not converge because near the maximum height the airspeed slows to a point lower than stall speed.

Table 5 Maximum lift-to-drag ratio for various aspect ratios

AR	$(L/D)_{\max}$
15	23.02
17	24.51
19	25.91
20	26.59
21	27.24
23	28.51
25	29.72

Table 6 Maximum lift-to-drag ratio for various C_{D_0} values

C_{D_0}	$(L/D)_{\max}$
0.015	30.70
0.017	28.84
0.019	27.28
0.020	26.59
0.021	25.95
0.023	24.79
0.025	23.78

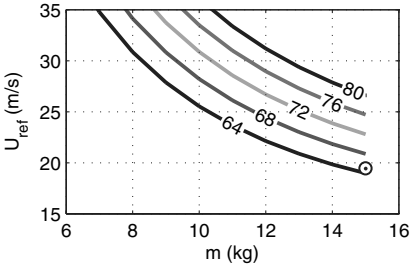

Fig. 13 Dynamic-soaring reference wind speed as a function of sailplane mass for various dwell speeds ranging from 64 to 80 m/s (baseline case shown as circle symbol).

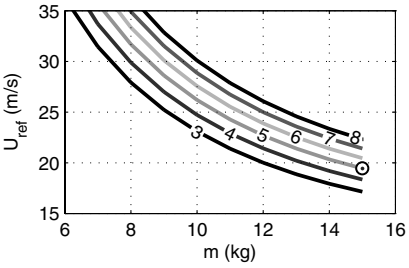

Fig. 14 Dynamic-soaring reference wind speed as a function of sailplane mass for various dwell heights ranging from 3 to 8 m (baseline case shown as circle symbol).

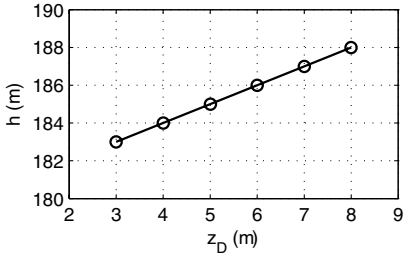

Fig. 15 Orbit maximum height with increasing dwell height z_D showing one-for-one correspondence.

C. Effects of Trajectory Parameters

The three main trajectory parameters used in this study are the initial height z_D, flight-path-angle parameter γ_1, and orbit radius r. With all aircraft parameters and other trajectory parameters fixed, the dwell height z_D has the direct effect of increasing the maximum altitude because it merely shifts the entire orbit up by the increment in z_D based simply on the fixed orbit shape defined by r and γ_1. However, moving the orbit up makes it less efficient because the sailplane does not benefit as much from the stronger wind shear close to the surface. This resulting effect on efficiency is clearly shown in Fig. 14, and Fig. 15 shows the simple one-for-one result of incremental higher maximum altitude with each increment in dwell height. It is worth noting that a dwell height of 3 m gives a wing tip clearance approaching 1.5 m, which is most likely beyond the skills of a pilot to manage reliably.

The effect of changing the flight-path-angle parameter is shown in Fig. 16. An increase in this parameter γ_1 causes the flight path angle to increase around the entire orbit, making it more inclined to the wind. As this orbit becomes more inclined, the maximum height is increased based on simply the geometry of the orbit, and this effect on height is shown in Fig. 17. The baseline is the bounding case for

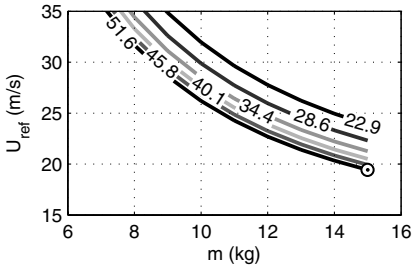

Fig. 16 Dynamic-soaring reference wind speed as a function of sailplane mass for various γ_1 values ranging from 22.9 to 51.6 deg (baseline case shown as circle symbol).

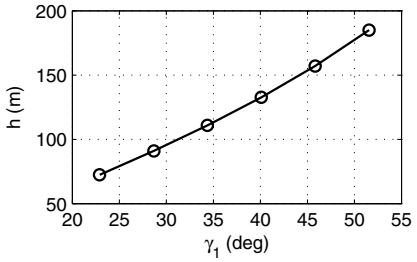

Fig. 17 Orbit maximum height with increasing orbit γ_1.

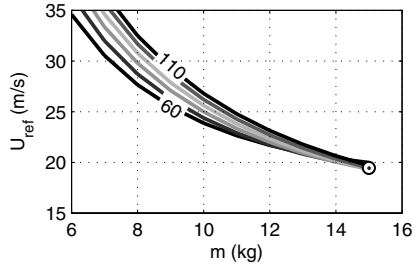

Fig. 18 Dynamic-soaring reference wind speed as a function of sailplane mass for various orbit radii ranging from 60 to 110 m (baseline case shown as circle symbol).

which the maximum altitude is 185.1 m, and from the results shown in Fig. 16, a further increase in the inclination of the orbit would not make it more efficient; i.e., it appears that the point of diminishing returns has been nearly reached with a minimum reference wind speed of 19.44 m/s (see Fig. 16) corresponding to the baseline case. With the dwell speed fixed for this two-parameter sweep, it is not surprising to find that for all cases the maximum speed is between 66 and 68 m/s near $\psi \approx 225$ deg. The maximum load factor stays between approximately 5 and 6.

Changes in the orbit radius are shown in Fig. 18. The orbit radius is the radius of the ground trace of the orbit measured in a frame of reference fixed to the aircraft. For the fixed flight-path-angle schedule [see Eq. (12)], a larger radius magnifies the orbit size, which results in a higher maximum orbit altitude, as shown in Fig. 19. As expected with the maximum speed set mainly by the dwell speed, the load factor in this case was driven by the radius. In particular, with these changes in radius, the maximum load for the 6-kg case changed from 9.2 to 5.6 for radii of 60 to 110 m, respectively. Correspondingly, for the 15-kg case, the load factor peaked at 5.6 to 5.1 for radii of 60 to 110 m.

The trend shown in Fig. 18 departs from those discussed so far. For mass on the lower side of the range, say, $m = 8$ kg, the orbit with the larger radius reaching a higher altitude (Fig. 19) requires a higher reference wind speed, but this same trend does not occur on the upper bound with $m = 15$ kg, in which the reference wind speed is approximately the same for any radii (any maximum height). Beyond this point (not shown), the curves cross over with the higher radius case becoming the most efficient. Or put somewhat differently, there appears a minimum for each curve, each in turn. This minimum point

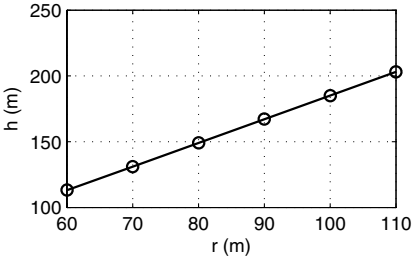

Fig. 19 Orbit maximum height with increasing orbit ground radius.

(which results in overlapping curves [19]) happens as a result of the tradeoff between parasite drag and induced drag. For the 60-m radius case (or any case for that matter), dynamic soaring is less efficient at lower wing loadings (lower mass) because of high parasite drag, whereas at higher wing loadings, it is less efficient because of high induced drag (with induced drag being proportional to span loading). At some point between having either high parasite drag or high induced drag, there is a minimum required reference wind speed corresponding to the minimum required wind shear that has been the subject of numerous other investigations on dynamic soaring, e.g., [4] and [6].

D. Achievable Characteristics for Extreme-Climb Dynamic Soaring

Based on the trends within the ranges considered, feasible (practical and realistic) sailplane characteristics and defining orbit parameters are given in Table 7. With these parameters, a reference wind speed of 12.97 m/s (29.02 mph) is required. All of these defining parameters are physically realizable. In fact, this wind speed U_{ref} corresponds to winds below the actual conditions given in Table 1. At these conditions with the dwell speed of 65 m/s, the wing chord average Reynolds number ranges from ≈200,000 near peak altitude to ≈530,000 at the dwell conditions. Moreover, the lift coefficient ranges from 0.16 to 1.12 from dwell to maximum altitude. Thus, taken together, extreme-climb dynamic soaring is quite possible.

V. Piloted Dynamic-Soaring Simulation

Extreme-climb dynamic soaring that resembles the preceding prescribed trajectories was simulated in a piloted real-time flight simulator. In the simulator, the full six-DOF equations of motion are solved using quaternions, and integration is carried out using a Runge–Kutta fourth-order scheme running at 300 Hz [23,24]. In the method, the aerodynamics are modeled based on a component buildup approach using table lookup for aerodynamic coefficients as functions of angle of attack and control surface deflections. Table lookup is also used for the vertical wind profile. Wind shear along the wingspan is captured by the method. The wind profile was constructed to match the low-shear case in Fig. 4 with the reference parameters given in Table 8.

The properties of the sailplane flown in the simulation are given in Table 9, and a perspective view is shown in Fig. 20. The 2.92-m

Table 7 Achievable sailplane characteristics and defining orbit parameters for extreme-climb dynamic soaring

Parameter	Value
m	15 kg (33.07 lb)
m/S (W/S)	41.67 kg/m^2 (136.56 oz/ft^2)
b	3 m (9.84 ft)
AR	25
e_o	0.9
C_{D_0}	0.015
$(L/D)_{\max}$	34.32
z_D	5 m (16.40 ft)
γ_1	0.9 (51.57 deg)
r	100 m (328.08 ft)

wingspan sailplane has characteristics somewhat similar to the preceding baseline with a high lift-to-drag ratio and high wing loading (Table 4). However, the wing loading is not as high as that in Table 7, and thus, the dynamic-soaring orbits are not expected to be as energetic (as high and as fast) as the extreme-climb scheduled trajectory path discussed in the preceding section.

The particular simulator used is the commercial FS One® RC flight simulator [25] that relies on the methods described in [23] and [24]. It allows for pilot input through a standard RC transmitter attached to a Universal Serial Bus (USB) adapter connected to the computer. The simulator includes flight dynamics recording features that allow for saving state data recorded during simulation to a file. The particular recorded flight shown here was flown in the simulator by the second author.

Figures 21 and 22 show the dynamic-soaring trajectory and orbit parameters for one nominal cycle. In this case, the cycle is defined to start and end at $\Delta\psi = -90$ and 270 deg, in which the absolute initial heading ψ is -108.06 deg. Again, the heading, $\Delta\psi$ in this case, is a surrogate time, or pseudo time. The total time for the segment is 14.73 s over a distance of 336.91 m, making the net downstream travel speed 22.87 m/s (51.16 mph). The flight was flown using a strategy that was found by trial and error to maximize the peak altitude as well as maximize downwind net travel speed.

At a glance, the piloted trajectory (Fig. 21) appears somewhat different than the scheduled trajectory for the baseline shown in Fig. 8, but for the most part, these differences are related to the amount of crab when flying crosswind. Because the airplane crabs into the wind by an amount that depends on the wind speed relative to the airspeed, plotting the effective time history vs absolute ψ (that is, from $\psi = -90$ to 270 deg) is not the best point of reference. Instead, the time history has been plotted so that it begins at a point in which the aircraft is traveling perpendicular to the wind and ends downstream at the same initial heading; that is, $\Delta\psi = 360$ deg later. These points are close to but not necessarily equal to the dwell conditions because the flight is piloted and hence not perfectly periodic. As a result, the initial and final conditions differ. Nevertheless, it is clearly one complete orbit and can be compared with the baseline orbit (Figs. 8 and 9).

Overall, there is generally less variation in the time histories for the piloted case in Fig. 22 as compared with the baseline in Fig. 9. In part, this is most likely a result of the piloted case being less energetic: lower maximum height and lower flight speed, as reflected in part by overall lower energy height.

As is similar to the baseline, it can be seen from the time history that there is a slight gain in energy height h_e that starts near $\Delta\psi \approx -80$ deg as the sailplane turns into the wind and starts to climb. For this period of time, the flight path relative to the ground takes a near vertical climb to the peak (extreme climb). As the peak is approached ($\Delta\psi \approx 80$ deg), the energy height then begins to plateau and then decay before starting to grow again with the downwind zoom that begins near $\Delta\psi \approx 120$ deg. Overall, the time history of the energy height is similar to that for the baseline, and this similarity results directly from the tradeoff between height and speed (potential energy and kinetic energy), which are also similar to the baseline.

Not surprisingly, with the piloted orbit shape being similar to the baseline, the time history for the flight path angle γ is similar, but the amplitude of the piloted case is overall lower because the orbit is not as inclined. The left aileron input δ_a driving full-span ailerons is minuscule throughout the entire orbit and pulsed for two brief periods to near -0.3 deg with small adjustments made for minor bank angle corrections to stay on orbit. Because these inputs are so small, their correspondence with changes in the bank angle ϕ is mostly imperceptible. The up-elevator input δ_e is small, but for the most part, the input is given to maintain the orbit and a positive load factor n (continuous turn). The correlation between up-elevator input and increased lift coefficient and load factor is as expected. Throughout the entire orbit, the load factor is modest and appears to be at a peak of $n \approx 5$ corresponding with the peak in up-elevator input and increased lift coefficient. As mentioned before, the initial and final values for this time history are not identical because of active pilot control input.

For the baseline orbit, the prescribed turn radius is held fixed, whereas, for the piloted case, the turn radius is a consequence of the pilot commands. Using Eq. (4), the instantaneous turn radius r can be computed from the time history, and the result is shown in Fig. 23. For this cycle, the average radius is 100.64 m, which happens to be almost the same as the baseline radius of 100 m (Table 4). The multiple spikes in the turn radius (flattening of the turn) from $\Delta\psi \approx 80$ to 180 deg correspond to reduced up-elevator input on the downwind leg (see Fig. 22). As mentioned, the flight was flown to also maximize downwind travel speed (besides maximizing height), and it was found that "stretching out" the downwind leg increased the downwind travel speed. The net increase in the turn radius during this

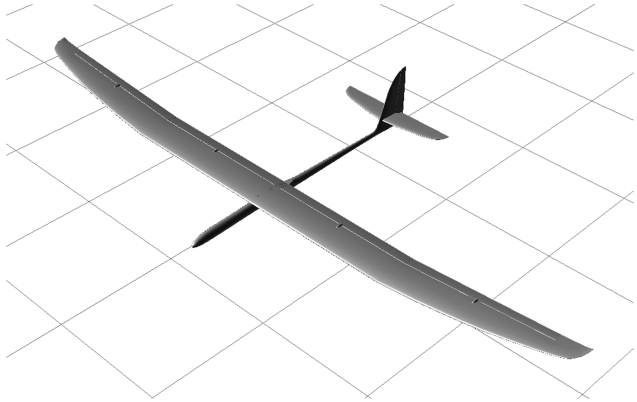

Fig. 20 Perspective view of the 2.92-m wingspan sailplane used in the piloted simulation demonstration (grid spacing is 0.5 m^2).

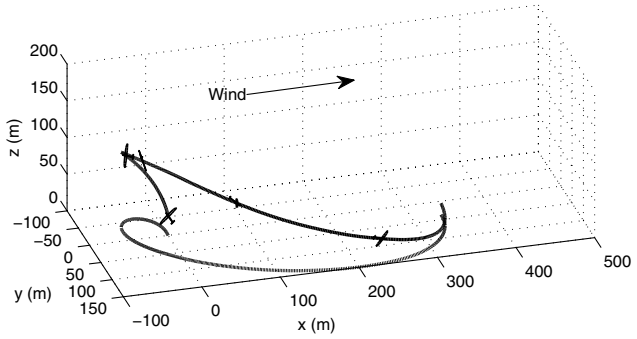

Fig. 21 Dynamic-soaring trajectory of a 2.92-m wingspan sailplane flown using the FS One flight simulator (sailplane magnified 10 times normal size and drawn every 3 s).

Table 8 Wind profile parameters for extreme-climb dynamic soaring

Parameter	Value
U_{ref}	15 m/s (33.55 mph)
z_{ref}	10 m (32.81 ft)
z_0	0.05 m (1.97 in)

Table 9 Sailplane parameters used in real-time piloted simulation demonstration

Parameter	Value
m	17.26 kg (38.05 lb)
I_{xx}	3.525 kg · m^2 (83.7 lb · ft^2)
I_{yy}	0.796 kg · m^2 (18.9 lb · ft^2)
I_{zz}	4.270 kg · m^2 (101.3 lb · ft^2)
m/S (W/S)	34.17 kg/m^2 (112.0 oz/ft^2)
b	2.92 m (9.58 ft)
AR	16.90
$(L/D)_{\max}$	≈34

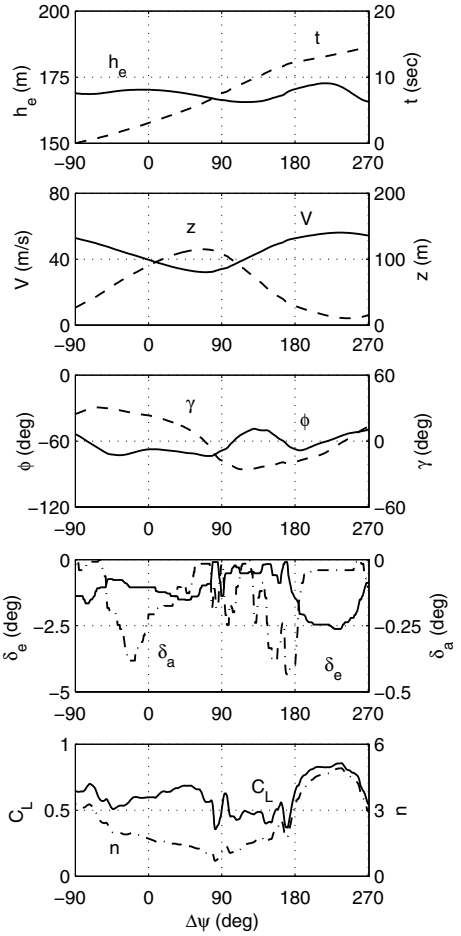

Fig. 22 Extreme-climb dynamic-soaring orbit parameters for one nominal cycle during the simulation (see Fig. 21).

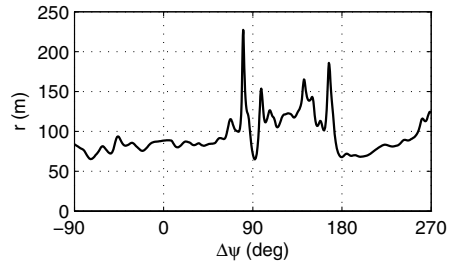

Fig. 23 Instantaneous orbit ground turn radius *r* computed from time history (see Fig. 22).

part of the orbit is a direct indication of the period in time during which the trajectory was adjusted to be less curved and directed more downwind.

The single dynamic-soaring orbit shown in Fig. 21 was extracted from the full longer flight shown in Fig. 24. The entire trajectory was piloted in real time using only dynamic soaring to stay aloft. The flight begins at an elevation of $z = 90.12$ m (295.67 ft) and an

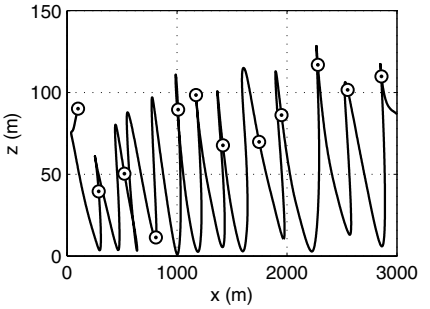

Fig. 25 Elevation history of flight shown in Fig. 24.

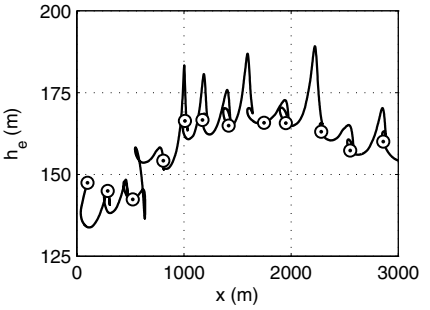

Fig. 26 Energy height history of flight shown in Fig. 24.

airspeed of 33.48 m/s (74.89 mph). Symbols are drawn every 15 s to give a sense of speed downwind. The full recording shown lasted 164.6 s over a total distance traveled of 2754.6 m giving an average downwind speed of 16.73 m/s (37.42 mph). The single orbit shown in Fig. 21 begins at $x = 1641.6$ m in this larger time history. Figure 25 shows the elevation history for the same flight with symbols again spaced 15 s apart.

What can be gleaned from the full flight is that, as expected, if one orbit can be successfully completed, a full continuous series can be completed indefinitely. More important, however, it does demonstrate that piloted dynamic soaring over open land is expected to be possible with the right combination of weather, wind, airplane characteristics, and pilot skills.

Another interesting element is that the sustained dynamic soaring does not need to begin from a full larger orbit; e.g., it can begin from straight and level flight, as with the piloted case shown in Fig. 24. Moreover, as Fig. 25 shows, the envelope of the peak heights builds over time from a point with initial conditions that are easily physically realizable. Figure 26 shows that the energy height is on average increasing until it reaches a relatively constant mean level once the sailplane reaches high altitudes at its peak, where the wind shear is reduced. Also, the orbit (Fig. 25) does not require flying over the full extent of the ground boundary layer, which is advantageous when one considers that in any long flight like this there will likely be ground obstructions that must be avoided to prevent collisions. Finally, after the orbit has been sustained with near regular periodicity, the elevation (maximum and minimum) fluctuates, illustrating that the trajectory is robust.

As a final comment, the piloted simulation supports the suggestion that dynamic soaring can be synchronized with the natural phugoid-

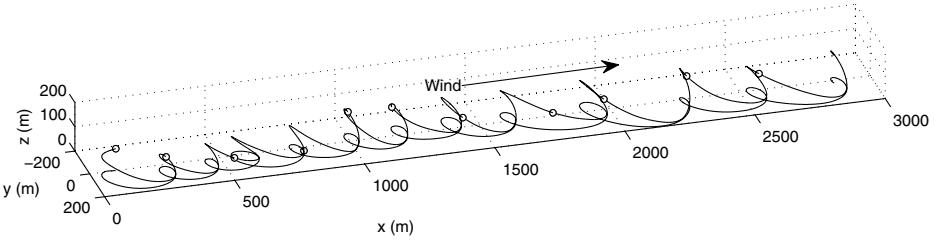

Fig. 24 Full 164.6 s flight that includes the single orbit shown in Fig. 21.

type motions [3]. Using the respective time-averaged airspeeds of 51.17 and 43.04 m/s for the prescribed trajectory baseline orbit (Fig. 8) and the piloted flight (Fig. 21) yields phugoid time periods $[T \approx \pi\sqrt{2}(V/g)]$ of 23.17 and 19.49 s as compared with the actual orbit times of 16.2 and 14.73 s, respectively. These differences in times between the longitudinal phugoid mode and the dynamic-soaring phugoid mode must be related to the nonlinear effects of dynamic soaring, that is, wind shear (energy extraction), significant angle-of-attack changes, and the fact that dynamic soaring involves turning. The common denominators between a longitudinal-flight phugoid and the dynamic-soaring phugoid are that they both involve a tradeoff between kinetic energy and potential energy and both happen over a relatively long period. Moreover, for the piloted case and supportive of the suggestion that dynamic soaring can be synchronized with the natural phugoid-type motion [3], it was found that the sailplane could be trimmed to fly the orbits with only minuscule (almost fixed) pilot input, as can be seen in the elevator and aileron inputs shown in Fig. 22.

VI. Conclusions

Based on the results presented in this paper, dynamic soaring with extreme climbs to high altitudes over open land in high (realistic)-wind conditions appears feasible. Both a point-mass prescribed trajectory simulation and a six-degree-of-freedom piloted simulation show that the achievement of dynamic soaring from the ground to near the edge of the atmospheric boundary layer (where the wind shear approaches zero) is an extension of the type of dynamic soaring performed by the albatross close to the sea. Significant differences are that the sailplane flight to high altitudes requires higher airspeeds (65 m/s) and higher load factors (6 to 9). Reference wind speeds between approximately 15–20 m/s (for $z_{\text{ref}} = 10$ m) are required for sailplanes with wingspans near 3 m with wing loadings in the range $W/S \approx 12$–30 kg/m^2 depending on the amount of wind shear. For such conditions, energy-conserving dynamic-soaring orbits from ground level to 120–180 m in wind shear appear possible. Finally, flight under these conditions requires little pilot workload with only minor pilot inputs required to maintain consistent and robust high-energy dynamic-soaring orbits over land.

References

[1] Rayleigh, L., "The Soaring of Birds," *Nature (London)*, Vol. 27, April 1883, pp. 534–535. doi:10.1038/027559a0

[2] Hendriks, F., "Dynamic Soaring," Ph.D. Dissertation, Univ. of California, Los Angles, CA, 1972.

[3] Hendriks, F., "Extraction of Flow Energy by Gliding in a Wind with Uniform Vertical Shear," Univ. of California, Rept. UCLA-ENG-7324, Los Angeles, California, 1973.

[4] Sachs, G., "Minimum Shear Wind Strength Required for Dynamic Soaring of Albatrosses," *Ibis*, Vol. 147, 2005, pp. 1–10. doi:10.1111/j.1474-919x.2004.00295.x

[5] Barnes, J. P., "How Flies the Albatross—The Flight Mechanics of Dynamic Soaring," SAE Paper 2004-01-3088, Nov. 2004.

[6] Lissaman, P., "Wind Energy Extraction by Birds and Flight Vehicles," AIAA Paper 2005-241, Jan. 2005.

[7] Denny, M., "Dynamic Soaring: Aerodynamics for Albatrosses," *European Journal of Physics*, Vol. 30, Jan. 2009, pp. 75–84. doi:10.1088/0143-0807/30/1/008

[8] Sachs, G., and da Costa, O., "Optimization of Dynamic Soaring at Ridges," AIAA Paper 2003-5303, Aug. 2003.

[9] Zhao, Y. J., "Optimal Patterns of Glider Dynamic Soaring," *Optimal Control Applications and Methods*, Vol. 25, May 2004, pp. 67–89. doi:10.1002/oca.739

[10] Akhtar, N., Whidborne, J. F., and Cooke, A. K., "Wind Shear Extraction Using Dynamic Soaring Techniques," AIAA Paper 2009-7734, 2009.

[11] Zhao, Y. J., and Qi, Y. C., "Minimum Fuel Powered Dynamic Soaring of Unmanned Aerial Vehicles Utilizing Wind Gradients," *Optimal Control Applications and Methods*, Vol. 25, May 2004, pp. 211–233. doi:10.1002/oca.744

[12] Gordon, R. J., "Optimal Dynamic Soaring for Full Size Sailplanes," M.S. Thesis, Dept. of Aeronautical and Astronautical Engineering, Air Force Inst. of Technology, Wright–Patterson AFB, OH, Sept. 2006.

[13] Wurts, J., "Dynamic Soaring," *Sailplane and Electric Modeler*, Vol. 3, No. 5, Aug.–Sept. 1998, pp. 52–53.

[14] Fogel, L., "Dynamic Soaring?," *Sailplane and Electric Modeler*, Vol. 4, No. 5, Jan. 1999, pp. 94–97.

[15] Sachs, G., and Mayrhofer, M., "Dynamic Soaring Basics: Part 1, Model Gliders and Ridges," *Sailplane and Electric Modeler*, Vol. 7, No. 10, Dec. 2002, pp. 32, 36–37.

[16] Sachs, G., and Mayrhofer, M., "Dynamic Soaring Basics: Part 2, Minimum Wind Strength," *Sailplane and Electric Modeler*, Vol. 8, No. 1, Jan. 2003, pp. 82, 84–85.

[17] Boslough, M. B. E., "Autonomous Dynamic Soaring Platform for Distributed Mobile Sensor Arrays," Sandia National Lab., Rept. SAND2002-1896, Albuquerque, NM, 2002.

[18] Parle, J., "Preliminary Dynamic Soaring Research Using a Radio Control Glider," AIAA Paper 2004-132, Jan. 2004.

[19] Sukumar, P. P., "Dynamic Soaring of Sailplanes in Open Fields," M.S. Thesis, Dept. of Aerospace Engineering, Univ. of Illinois at Urbana–Champaign, Urbana, IL, 2008.

[20] Deittert, M., Richards, A., Toomer, C. A., and Pipe, A., "Engineless Unmanned Aerial Vehicle Propulsion by Dynamic Soaring," *Journal of Guidance, Control, and Dynamics*, Vol. 32, No. 5, Sept.–Oct. 2009, pp. 1446–1457. doi:10.2514/1.43270

[21] Stevens, B. L., and Lewis, F. L., *Aircraft Control and Simulation*, 2nd ed., Wiley, New York, 2003, pp. 71–99.

[22] Stull, R., *An Introduction to Boundary Layer Meteorology*, Atmospheric and Oceanographic Sciences Library, Vol. 13, Springer, 2009, pp. 376–381.

[23] Selig, M. S., "Modeling Full-Envelope Aerodynamics of Small UAVs in Realtime," AIAA Paper 2010-7635, Aug. 2010.

[24] Selig, M. S., "Modeling of Propeller Aerodynamics and Slipstream Effects on UAVs in Realtime," AIAA Paper 2010-7938, Aug. 2010.

[25] FS One, Precision RC Flight Simulator, Ver. 2.0, Software Package, InertiaSoft, Champaign, IL, 2012, http://www.fsone.com/products/fs-one-v2 [retrieved 15 Nov. 2012].